



Excellent detection of H₂S gas at ppb concentrations using ZnFe₂O₄ nanofibers loaded with reduced graphene oxide

Nguyen Van Hoang^{a,b}, Chu Manh Hung^a, Nguyen Duc Hoa^a, Nguyen Van Duy^a, Inkyu Park^c,
Nguyen Van Hieu^{d,e,*}

^a International Training Institute for Materials Science (ITIMS), Hanoi University of Science and Technology, Hanoi, Viet Nam

^b Department of Materials Science and Engineering, Le Quy Don Technical University, Hanoi, Viet Nam

^c Inkyu Park, Department of Mechanical Engineering, Korea Advanced Institute of Science and Technology (KAIST), Daejeon, South Korea

^d Faculty of Electrical and Electronic Engineering, Phenikaa Institute for Advanced Study (PIAS), Phenikaa University, Yen Nghia, Ha-Dong district, Hanoi, 10000, Viet Nam

^e Phenikaa Research and Technology Institute (PRATI), A&A Green Phoenix Group, 167 Hoang Ngan, Hanoi, 10000, Viet Nam

ARTICLE INFO

Keywords:

RGO
ZnFe₂O₄
Nanofibers
Electrospinning
H₂S
Gas sensors

ABSTRACT

Cost-effective fabrication of sensors and detection of ultralow concentrations of toxic gases are important concerns for environmental monitoring. In this study, the reduced graphene oxide (RGO)-loaded ZnFe₂O₄ nanofibers (ZFO-NFs) were fabricated by facile on-chip electrospinning method and subsequent heat treatment. The multi-porous NFs with single-phase cubic spinel structure and typical spider-net morphology were directly assembled on Pt-interdigitated electrodes. The diameters of the RGO-loaded ZFO-NFs were approximately 50–100 nm with many nanograins. The responses to H₂S gas showed a bell-shaped behaviour with respect to RGO contents and annealing temperatures. The optimal values of the RGO contents and the annealing temperatures were found to be about 1.0 wt% and 600 °C, respectively. The response of the RGO-loaded ZnFe₂O₄ NFs to 1 ppm H₂S gas was as high as 147 at 350 °C while their cross-gas responses to SO₂ (10 ppm), NH₃ (100 ppm), H₂ (250 ppm), C₃H₆O (1000 ppm), and C₂H₅OH (1000 ppm) were rather low (1.8–5.6). The high sensor response was attributed to formation of a heterojunction between RGO and ZnFe₂O₄ and due to the fact that NFs consisted of many nanograins which resulted in multi-porous structure and formation of potential barriers at grain boundaries.

1. Introduction

The detection of toxic gases using nanoscale materials has attracted much attention as this is widely realized as one of the most promising fields for nanotechnology to have significant impacts on industry and society. Hydrogen sulfide (H₂S) is an extremely toxic gas which can cause harmful human health effects, even at low concentrations [1–6]. Therefore, many sensing nanomaterials have been developed for the detection of H₂S gas, especially at ppb level [7–9]. Among those materials, nanostructured semiconductor metal oxides (SMO) are cost-effective and have facile large-scale fabrication for H₂S gas sensors [10]. SMO loaded with RGO are a potential material for chemiresistive sensors because of their outstanding combined properties. Recent works have indicated that RGO-loaded SMO exhibited great enhanced H₂S gas-sensing properties compared to pure SMO because of the formation of a heterojunction between RGO and SMO [11–14]. For instance, Shi

et al. [11] prepared RGO/h-WO₃ composites with different contents of RGO (0–7.2 wt%) by hydrothermal method. The sensor based on 3.8 wt% RGO/h-WO₃ composites exhibited the best gas sensing response to H₂S. The sensitivity of the sensor was about 168.58 to 40 ppm H₂S at optimal temperature of 330 °C, which was 3.7 times higher than that of pure WO₃ at the same working conditions.

The enhanced sensing properties of the RGO-loaded SMO NFs sensors fabricated by electrospinning which is a practical method because of its economy, simplicity, and flexibility [15,16] were also reported in various works [17–23]. For example, Guo et al. [18] investigated the effects of RGO weight ratios (0–3%) on acetone sensing properties of the RGO-decorated α-Fe₂O₃ NF sensor. The results showed that the response of the 1.0 wt% RGO-decorated α-Fe₂O₃ NF sensor to 100 ppm acetone gas at the optimal operating temperature was about four times higher than that of pure α-Fe₂O₃ NFs. Kim et al. also reported the enhanced sensing response of the sensors based on RGO-loaded SMO NFs

* Corresponding author at: Phenikaa Institute for Advanced Study (PIAS), Phenikaa University, Yen Nghia, Ha-Dong district, Hanoi, 10000, Viet Nam.

E-mail address: hieu.nguyenvan@phenikaa-uni.edu.vn (N. Van Hieu).

<https://doi.org/10.1016/j.snb.2018.11.157>

Received 9 August 2018; Received in revised form 16 November 2018; Accepted 28 November 2018

Available online 29 November 2018

0925-4005/ © 2018 Elsevier B.V. All rights reserved.

[19,20,22,23]. Accordingly, the RGO-loaded ZnO NF sensor showed a bell-shaped behaviour response to NO₂ gas with respect to the weight ratio of RGO (0–1.04%) [22]. The sensor containing 0.44 wt% RGO showed the highest response to 5 ppm NO₂ at 400 °C, much higher than that of pure ZnO NFs. The enhanced sensing properties of typical RGO-loaded SMO NF sensors were attributed to grain boundary effects and formation of a heterojunction between RGO and SMO [19,20,22,23]. Choi et al. [13] synthesized RGO-functionalized SnO₂ NF sensor two-step method in which SnO₂ NFs were prepared by electrospinning, then mixed to RGO on Al₂O₃ sensor substrates. The sensor exhibited response of 33.7 to 5 ppm H₂S at operating temperature of 200 °C, 7.6 times higher than the response of the pristine SnO₂ at the same working conditions. However, no authors have reported about enhanced H₂S sensing response of the sensor based on RGO loaded-SMO NFs which were prepared on-chip by electrospinning for H₂S detection, especially at ppb level.

Spinel ZnFe₂O₄ (ZFO), an n-type SMO characterized by a normal spinel structure where tetrahedral sites were occupied by divalent Zn²⁺ cations and octahedral sites by trivalent Fe³⁺ cations [5], has recently attracted considerable attention as a promising candidate for detecting H₂S gas. Up to present, there have been no reports on incorporation of RGO in ZFO NFs for enhanced H₂S gas-sensing performance although ZnFe₂O₄-RGO composite nanofibers (NFs) for application as anode materials for enhanced performance of lithium-ion batteries were prepared by electrospinning and then incorporated with RGO by solvothermal method [15]. The tested results of the batteries showed that the nanocomposite material could remarkably improve rate capability and cycling stability. Liu et al. [24] also prepared RGO-ZFO composites with different weight ratios of RGO (0–3 wt%) via solvothermal method for enhanced acetone gas sensing. The results showed that RGO could improve the sensing properties of the sensors based on RGO-ZFO composites. The response of the 0.125 wt% RGO-loaded ZFO composite to 1000 ppm acetone at 275 °C was much higher than that of the bare ZFO sensor. Otherwise, the influences of heated treatments on the gas-sensing properties of NFs were reported in several works [25–27]; however, these effects on the RGO-loaded ZFO NF sensors have not been mentioned. Thus, a unique fabrication process of RGO-loaded ZFO NF sensors via facile on-chip electrospinning method for excellent detection of H₂S gas down to the ppb level was introduced in this study. The advantages of this method included: (1) combination of synthetic sensing material and sensor fabrication in one step; (2) favourability for large-scale sensor fabrication; and (3) better reproducible fabrication of NFs-based sensors as compared with the two-step method. In addition, the effects of RGO content and annealing temperature on the H₂S gas-sensing performance of RGO-load ZFO NF sensors were also investigated in detail.

2. Experimental

The on-chip preparation process of RGO-loaded ZFO NFs is described in detail in Text S1-S2 (Supporting Information). In brief, reduced graphene oxide (RGO) was reduced from graphene oxide (GO) which was synthesized from graphite power by Hummers method. Then, RGO-loaded ZFO of various contents (0–1.5 wt%) were fabricated on chip by electrospinning. Finally, the as-prepared sensors were calcined to form RGO-loaded ZFO NFs.

Raman spectroscopy, thermogravimetric and differential thermogravimetric analysis, field emission scanning and transition electron microscopies, X-ray spectroscopy, and X-ray diffraction were employed for material characterizations. More detail can be found out in Text S3 (Supporting Information)

The flow-through technique has employed for investigation of gas-sensing properties of ZFO and RGO-loaded ZFO NF gas sensors. The sensor response (*S*) was calculated by the ration of R_a/R_g (for reducing gases) or R_g/R_a (for oxidizing gases), where R_a and R_g were the resistances of the sensors in the dry air and tested gas, respectively. The

response-recovery time (τ_{resp} & τ_{recov}) were defined as the time taken by the sensor to reach 90% of its saturation after exposure to H₂S and air, respectively. More detail can be found out in Text S4 (Supporting Information)

3. Results and discussion

3.1. Microstructure characterizations

Figure S1 (Supporting Information) exhibits the analysis results of as-synthesized RGO. The XRD patterns in Figure S1a show two broad diffraction peaks at (002) and (100) of RGO. The pattern of the broad peaks indicates the production of significantly exfoliated RGO sheets [28]. The XRD results are similar to those of previous studies [22,29–31]. The Raman spectrum of RGO contains D and G bands (at 1337 and 1595 cm⁻¹, respectively) with an increased D/G intensity ratio of 1.25 (Figure S1b). This ratio value is consistent with most chemical reduction reports [32–38]. The D/G intensity ratio measures disorder degree and sp² domain size of RGO [39,40]. The thermal stability of RGO was investigated through TGA and DTG, as shown in Figure S1c. The weight loss below 100 °C is due to the removal of absorbed water molecules. The weight loss around 200 °C is due to pyrolysis of the labile oxygen-containing function groups [34,36,41]. The RGO show very high thermal stability with a total weight loss of 30% at the temperature below 800 °C. These results confirm that RGO are synthesized successfully by the reduction of RGO with ascorbic acid.

Fig. 1a–d shows morphologies and microstructures of RGO-loaded ZFO NFs with different amounts of RGO. It is obvious that the morphologies and microstructures of NFs are not significantly affected by the change of the RGO content (0–1.5 wt%). The average diameter of the NFs is 50–100 nm with rough surfaces because the NFs consist of many nanograins. The presence of RGO cannot be found from FE-SEM images of RGO-loaded ZFO NFs since the amount of RGO in the NFs is relatively little [11]. The insets corresponding to low magnification images show typical uniform spider-net-like distributions of NFs on the substrate.

The effects of annealing temperature on morphologies of 1.0 wt% RGO-loaded ZFO NFs are shown in Fig. 2. At a low annealing temperature of 400 °C, the NF surfaces are quite smooth because the nanograins are small. When the annealing temperature increases, NF surfaces become rough because of increased nanograin size. At a high annealing temperature of 700 °C, nanograins become much larger and even some thin nanofibers look like bamboos since the grain diameter is almost equal to the nanofiber diameter. The nanograin growth at high annealing temperature is targeted at reducing free energy in the system caused by decrease in total grain boundary area [25–27].

The chemical composition and crystal structure of 1.0 wt% RGO-loaded ZFO NFs are exhibited in Fig. 3. The XRD patterns show the sharp peaks corresponding to reflection planes (111), (220), (311), (222), (400), (422), (511), and (440) (Fig. 3a). The XRD results are consistent with the cubic spinel structure of ZFO (JCPDS card no. 89-7412). The average nanograin size calculated by the Scherrer equation with the highest peak of (311) diffraction plane is approximately 20 nm. Noticeably, there are no obvious diffraction peaks of RGO, which is similar to previous reports [11,24,42,43]. The presence of RGO in NFs is confirmed by EDX and TEM. The EDX spectrum indicates the presence of C, Fe, Zn and O elements from the NFs (Fig. 3b). Si comes from the Si/SiO₂ substrate. It can be seen that there are no impurities integrated in the synthesized NFs. The Fe, Zn content is quite small compared to Si content as predicted, which is due to the NFs dispersed across the substrate with a low density as shown in Fig. 1.

The morphologies and structures of 1.0 wt% RGO-loaded ZFO NFs are further examined in Fig. 4. The NFs with the diameter of 50–100 nm possess a multi-porous nanostructure because they comprise many nanograins with an average grain size of approximately 20 nm. The presence of RGO nanosheets on the NF surface is shown in

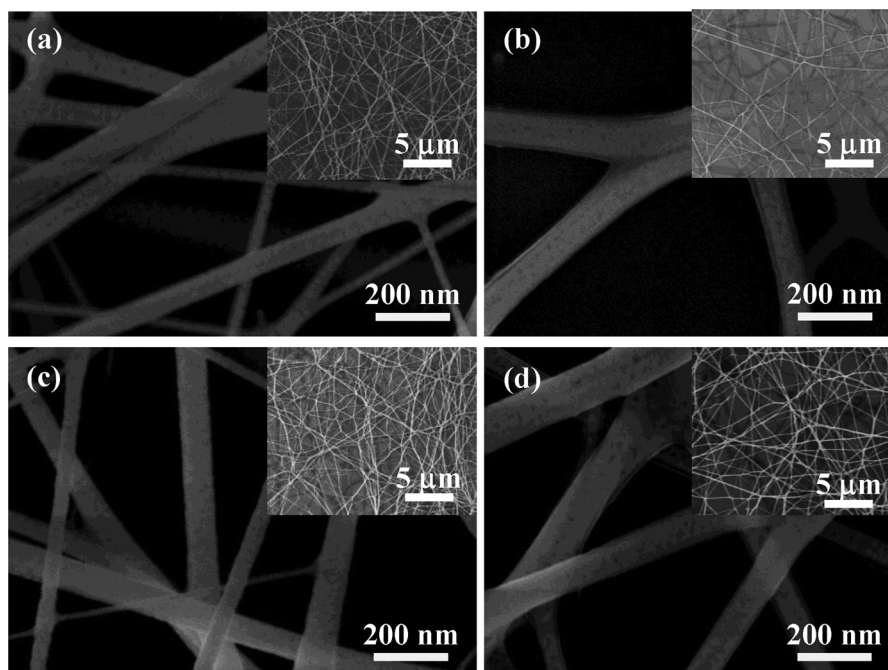


Fig. 1. FESEM images of the ZnFe_2O_4 NFs loaded with RGO at various contents: 0 (a), 0.5 (b), 1 (c) and 1.5 wt.% (d).

Fig. 4b. These morphologies are relevant to the above-mentioned FESEM, XRD, and EDX. The sharp-contrast spot patterns in the selected area electron diffraction (SAED) image depict the well-crystallized RGO-loaded ZFO NFs. The diffraction rings with d -spacing consistent with XRD results confirm the polycrystalline nature of the single-phase cubic spinel structure (Fd3m) of ZFO. The HRTEM in Fig. 4d exhibits parallel lattice fringes, which indicate a good crystalline structure. The spaces between lattice fringes are measured to be approximately 0.49 nm corresponding to the interplanar spacing of (111) lattice plane cubic spinel structure of ZFO, which is confirmed by fast Fourier transform (FFT) in the inset of Fig. 4d. All of the above-analysed results prove that well-crystalline RGO-loaded ZFO NFs are successfully fabricated by electrospinning.

3.2. Gas-sensing properties

The transient resistances to H_2S at 350°C of the RGO-loaded ZFO NFs sensors with different mixing ratios are shown in Fig. 5a–d. Both ZFO and RGO-loaded ZFO NF sensors show a typical n -type sensing behaviour (i.e. a resistance decrease by the reducing gas, H_2S). This reveals that the conduction in the RGO-loaded ZFO NFs is dominated by n -type ZFO nanograins. Fig. 5e–f shows the response and resistance of the RGO-loaded ZFO NF sensors as a function of RGO content. As presented in Fig. 5e, the sensor response reaches a maximum at 1.0 wt% RGO when the RGO content changes from 0 to 1.5 wt%. At a working temperature of 350°C , the response of the 1.0 wt% RGO-loaded ZFO NF sensor to 1 ppm H_2S gas is about 147, which is about 1.5 times higher than that of pure ZFO NFs in the same conditions. This sensing

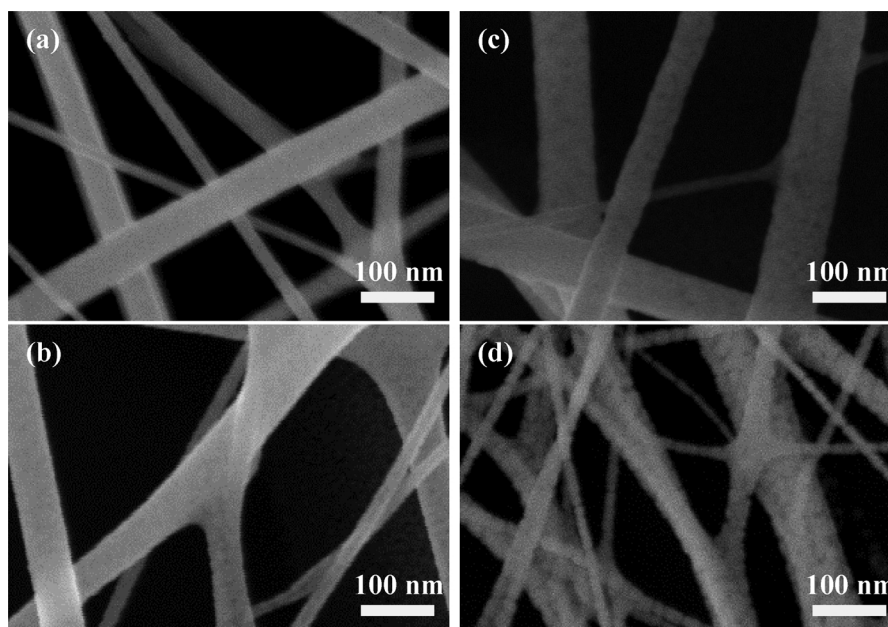


Fig. 2. FESEM images of 1%wt RGO-loaded ZnFe_2O_4 NFs calcined at (a) 400°C (b) 500°C (c) 600°C (d) 700°C for 3 h in air.

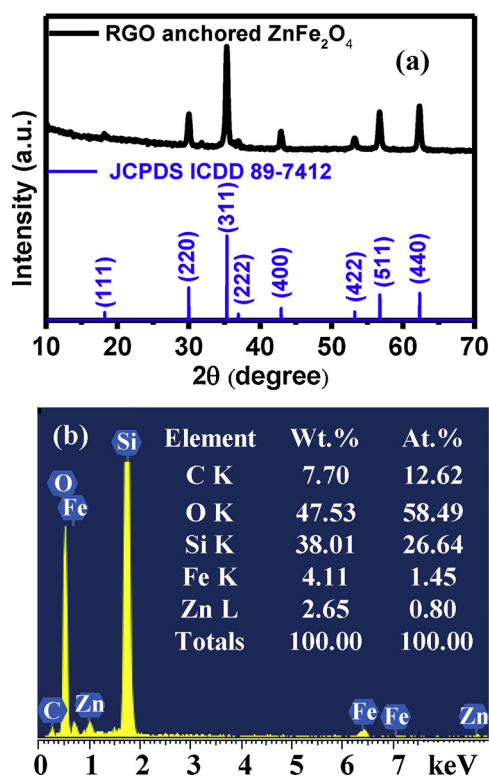


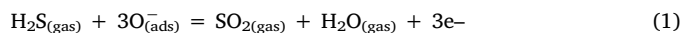
Fig. 3. XRD patterns (a) and EDX spectrum (b) of 1%wt RGO-loaded ZnFe_2O_4 NFs annealed at 600°C for 3 h in the air.

performance is much better than that of spinel ferrite oxide semiconductor gas sensors as previously reported [5]. Specifically, the RGO-load ZFO NF sensors can detect H_2S gas at concentrations as low as 0.1 ppm with a response of about 4.6. Such H_2S sensing ability has not been reported in the literature for SMO-based gas sensors [6,9].

The response and recovery times of the RGO-loaded ZFO NF sensors as functions of RGO content are shown in Fig. 5g. The recovery time increases when the RGO weight percentage increases between 0 and 1.0% due to increase in the amount of absorbed H_2S gas. However, when the RGO concentration is further increased to 1.5 wt%, the individual conducting path is formed, which causes increased electron mobility and decreased recovery time of the sensor. Meanwhile, the response time of the sensor does not change so much when RGO content changes. The response time of all RGO-load ZFO NF sensors is quite short, below 10 s.

These above-mentioned gas-sensing results can be explained by gas-sensing mechanisms as summarized in Fig. 6. It is possible that the formation of an RGO/ZFO heterojunction and ZFO grain boundaries have contributed to the excellent sensing behaviour of the sensors based on RGO-loaded ZFO NFs. As illustrated in Fig. 6a, the Fermi levels among ZFO nanograins are equal while the Fermi energy level of *n*-ZFO is supposed to be lower than that of *p*-RGO. In order to equate the Fermi levels, electrons would be transferred from RGO to ZFO at equilibrium, leading to formation of the potential barrier at the heterojunctions and the bending of energy levels (Fig. 6b). When sensors are exposed to air as shown in Fig. 6c, oxygen molecules are adsorbed on the surfaces of the NFs and then diffused along the grain boundaries. Oxygen molecules capture electrons from the conduction band to form oxygen ions (most O^- or O^{2-} at high working temperatures). As a result, two different depletion regions and potential barriers are formed in RGO-loaded ZFO NFs. One is at the heterojunctions between RGO and ZFO and another is at the boundaries of ZFO nanograins. When H_2S gas is introduced in Fig. 6d, H_2S molecules react with adsorbed oxygen ions (reactions 1–2) [3,44], which releases electrons back to the

conduction band and consequently contracts the depletion regions and potential barriers at the heterojunctions and grain boundaries; resulting in decreased resistance of the sensors. The *n*-type sensing behaviour also confirms that there is not enough RGO to form another conducting channel and the sensors based on RGO-loaded ZFO NFs express the *n*-type sensing characteristics of bare ZFO NFs base.



In addition, as shown in Fig. 6b, the formation of ohmic junctions between RGO sheets and ZFO nanograins makes ZFO become more *n*-type than the original state, leading to reduced energy barrier between ambient gas and ZFO [22,28,45]. The reduction of the energy barrier makes it easy for oxygen molecules to be absorbed on the ZFO NF surfaces, resulting in expanded depletion regions and increased sensor resistances (Fig. 5f). As a consequence, the modulation of sensor resistance increases when the sensors are exposed to reducing H_2S gas; therefore, the sensor response increases. Furthermore, the presence of RGO and RGO/ZFO interfaces in RGO-loaded ZFO NFs can lead to additional active gas-adsorption sites such as vacancies, defects, and oxygen functional groups; this consequently enhances the sensor response [46,47]. However, when the RGO concentration goes up to 1.5 wt%, the sensor response decreases because RGO sheets connect together to form an individual conducting path, which decreases overall sensor resistance (Fig. 5f). As a result, exposure of the sensor to H_2S gas also decreases the resistance modulation and results in a weaker sensor response.

In the present work, the H_2S sensing properties of the RGO-loaded ZFO NF sensors were also investigated at different working temperatures. The 1.0 wt% RGO-loaded ZFO NF sensor exhibiting the best response to H_2S was chosen for this investigation. The measured transient responses at working temperatures ranging from 350 to 450°C are shown in Fig. 7a-c. The *n*-type sensing behavior to H_2S was observed for the working temperatures. The response of the 1.0 wt% RGO-loaded ZFO NF sensors as functions of H_2S concentrations for different working temperatures is depicted in Fig. 7d. The sensor response increases with increased H_2S concentration from 0.1 to 1 ppm. Especially, the response significantly increases with an increase in gas concentration at 350°C . It is very interesting that the response decreases with an increase in working temperatures from 350 to 450°C , which is the same as that of pure ZFO NF sensors in our previous work [48]. This indicates that the loading of RGO in the NFs do not affect the working temperature. The response increases because the amount of H_2S molecules in absorption, diffusion, and reaction becomes greater with increased H_2S concentration. Meanwhile, the response decreases because of enhanced desorption with increased working temperature. In addition, the height of potential barriers among nanograins between RGO and ZFO NFs decreases with increased working temperature, resulting in decreased sensor response. The response-recovery time of the 1.0 wt% RGO-loaded ZFO NF sensor as functions of H_2S gas concentrations and working temperatures are shown in Fig. 7e and 7f, respectively. When H_2S gas concentrations increase from 0.1 to 1 ppm, the response time shortens because of reduced time for H_2S adsorption on active sites of NFs; meanwhile, the recovery time lengthens due to the longer time for H_2S gas desorption process. Conversely, the recovery time decreases with increased working temperature because of quicker H_2S gas desorption. The response time remains almost unchanged for all working temperatures. The sensor response increases when the working temperature is further decreased (see Figure S2a-b in Supporting Information). However, at lower working temperatures, the sensor resistance rapidly increases, and recovery time is too long (thousands of seconds) despite of unchanged response time (see Figure S2a-b in Supporting Information). At working temperature of 250°C , resistance and recover time of the sensor are $456\text{ M}\Omega$ and 1504 s , respectively. Therefore, working temperatures between 350 and 450°C are selected

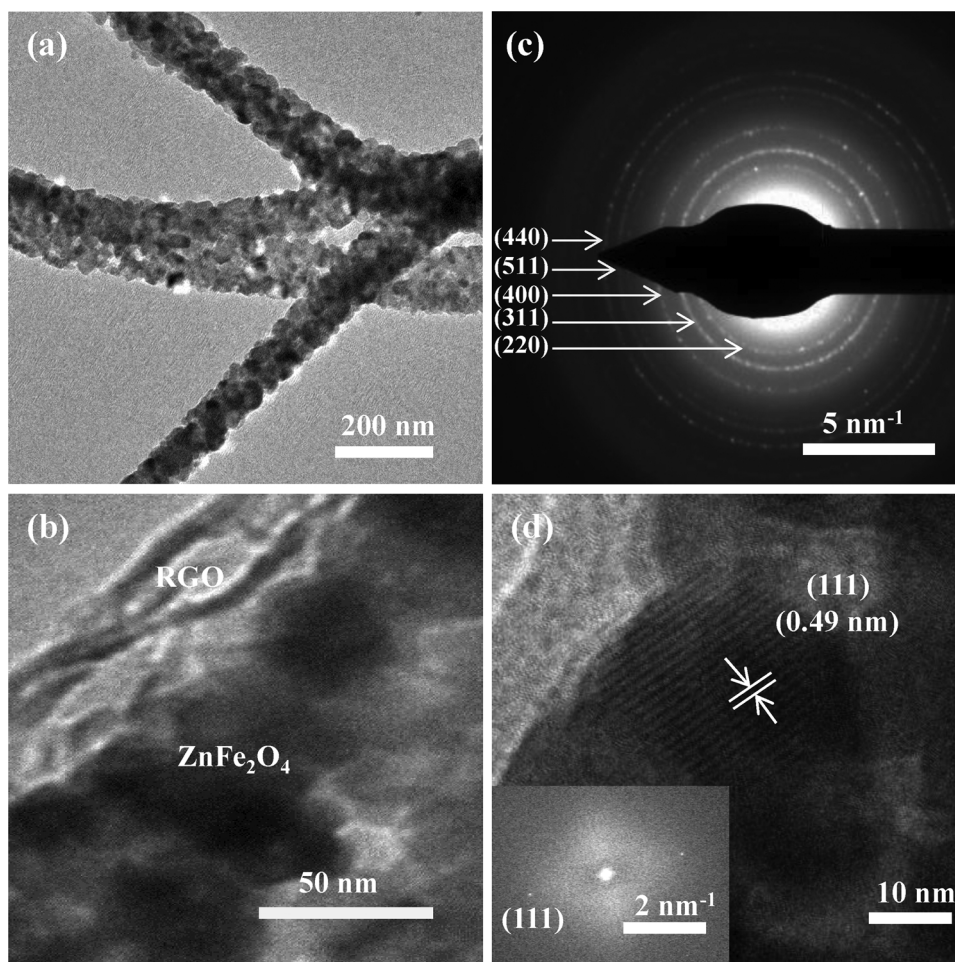


Fig. 4. TEM images at different magnifications (a–b), SAED pattern (c), and HRTEM image (d) with corresponding fast Fourier transform (FFT) inset image of 1%wt RGO-loaded ZnFe₂O₄ NFs annealed at 600 °C for 3 h in the air.

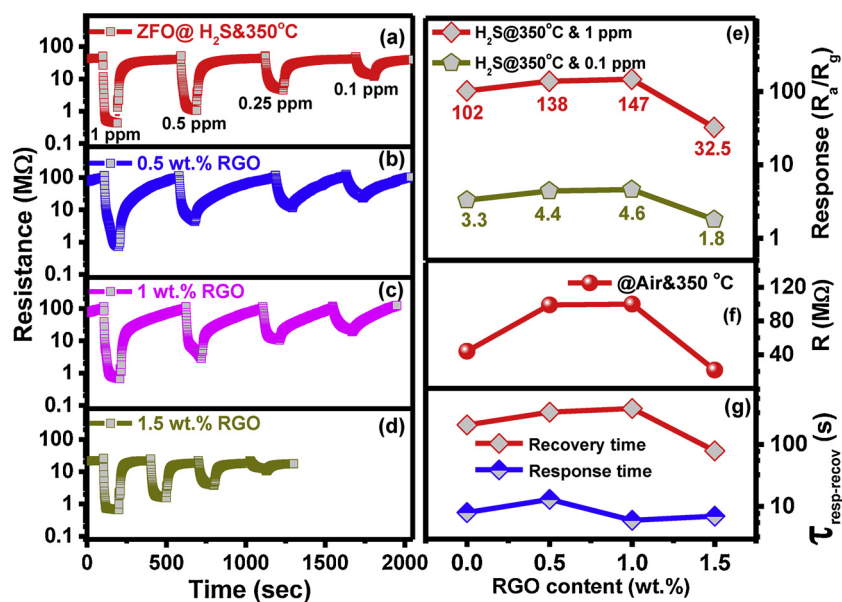


Fig. 5. H₂S sensing transients of ZnFe₂O₄ NF sensors loaded with different RGO contents: 0 (a), 0.5 (b) 1.0 (c) and 1.5 wt.% (d). Gas response (e), sensor resistance (f) and response-recovery time (g) as a function of RGO content at working temperature of 350 °C.

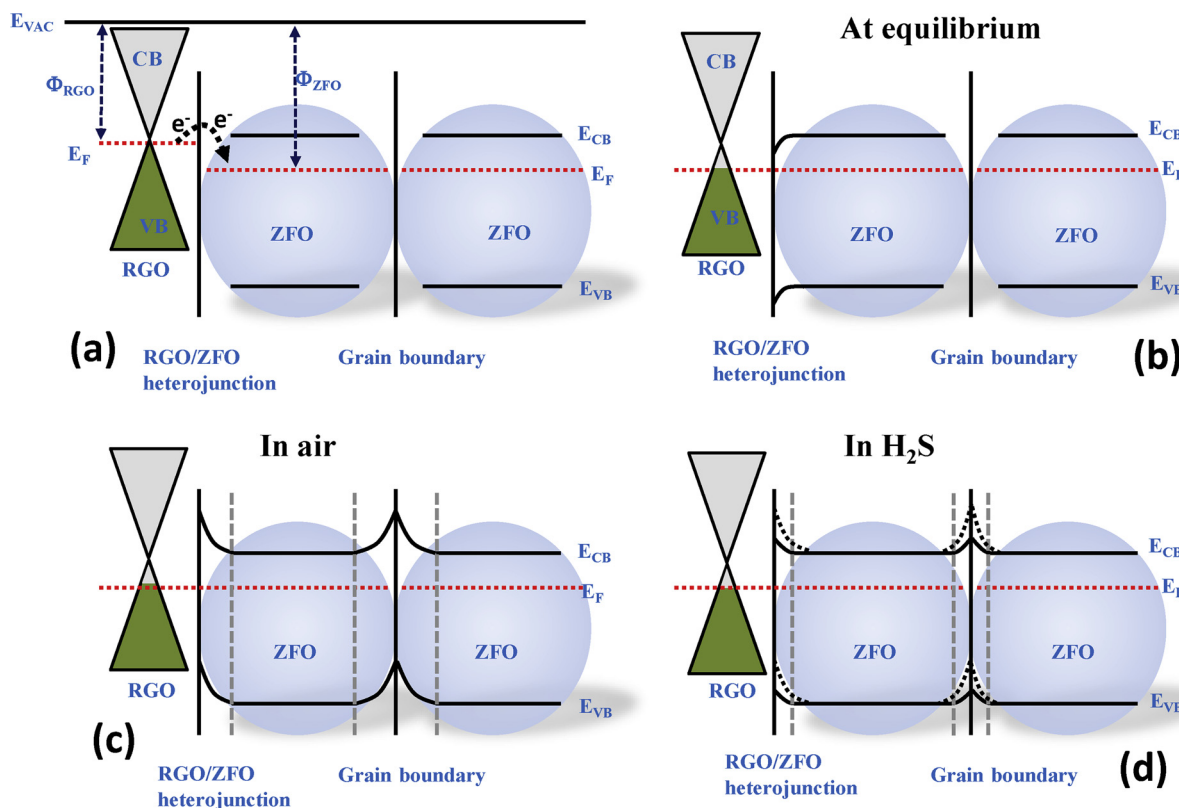


Fig. 6. Schematic of the proposed H₂S sensing mechanism of RGO-loaded ZFO NFs; band diagram of RGO and ZFO (a) at equilibrium (b) in air exposure (c) and in H₂S gas exposure (d).

to characterized gas-sensing properties with reasonable gas response, resistance and recovery time of the sensors.

The heat treatment directly influences the nanograin size and crystallinity of SMO NFs and these factors are strongly attributed to the gas sensing properties of the NFs. Thus, the effects of annealing temperature on the H₂S gas-sensing performance of the 1.0 wt% RGO-loaded ZFO NF sensor were worth investigating; the results are depicted in Fig. 8. The transient responses of 1.0 wt% RGO-loaded ZFO NFs

calculated at different annealing temperatures (400 – 700 °C) to 0.1 – 1 ppm H₂S gas at the working temperature of 350 °C are shown in Fig. 8a – d. All transient responses show an n-type sensing behaviour to reducing H₂S gas. The responses to H₂S concentration of 0.1 – 1 ppm as functions of annealing temperatures are exhibited in Fig. 8e. When the annealing temperature increases from 400 to 700 °C, the responses reach a maximum at 600 °C for all H₂S concentrations because of the inverse effects of nanograin size and crystallinity with increased

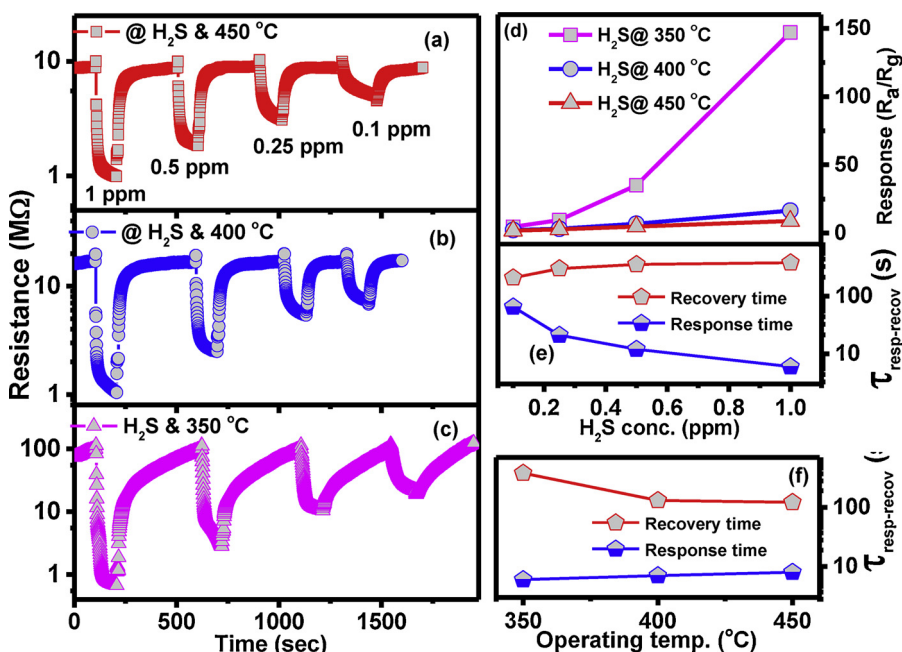


Fig. 7. H₂S sensing transients of 1% wt RGO-loaded ZnFe₂O₄ NF sensors measured at different operating temperatures of 450 °C (a), 400 °C (b) and 350 °C (c). Gas response as a function of H₂S gas concentration at different working temperatures (d), and response-recovery time as a function of H₂S concentrations (e) and operating temperatures (f).

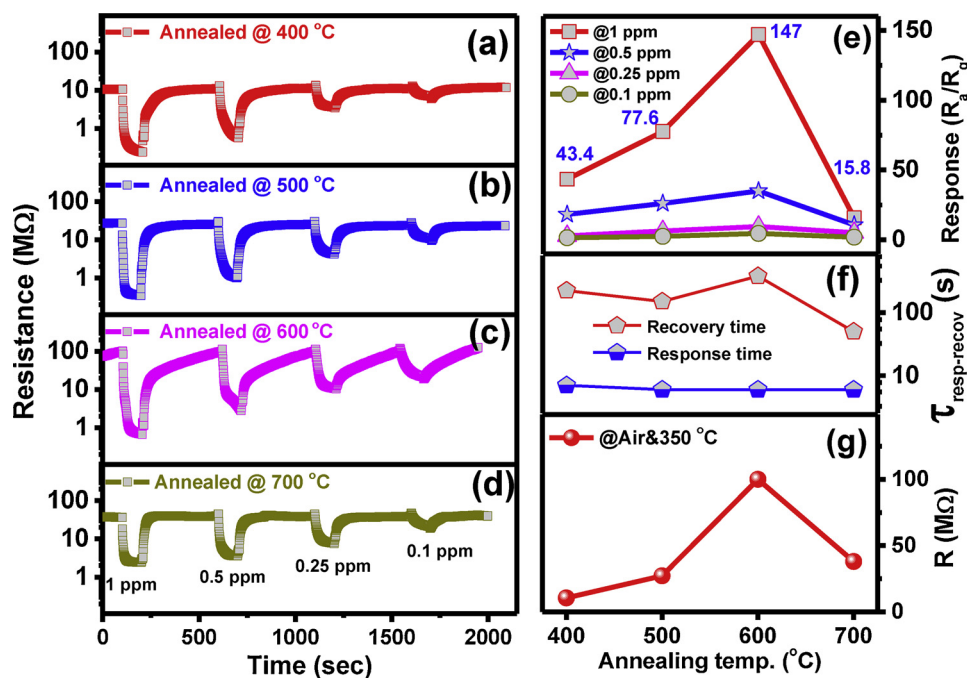


Fig. 8. H₂S sensing transients of 1.0 wt.% RGO –loaded ZnFe₂O₄ NF sensors at different annealing temperatures of 400 (a), 500 (b) 600 (c) and 700 °C (d). Gas response (e), sensor resistance (f) and response-recovery time (g) as a function of annealing temperatures at working temperature of 350 °C.

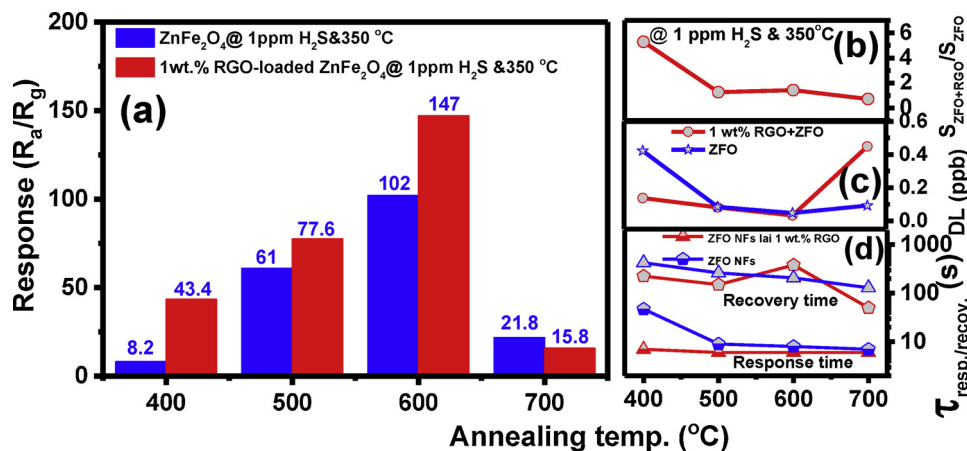


Fig. 9. Comparison of response (a), change level of response (b), detection limit (DL) (c) and response-recovery time (d) of bare-ZFO and 1%wt. RGO-loaded ZnFe₂O₄ NF sensors to 1 ppm H₂S gas at 350 °C as a function of annealing temperatures.

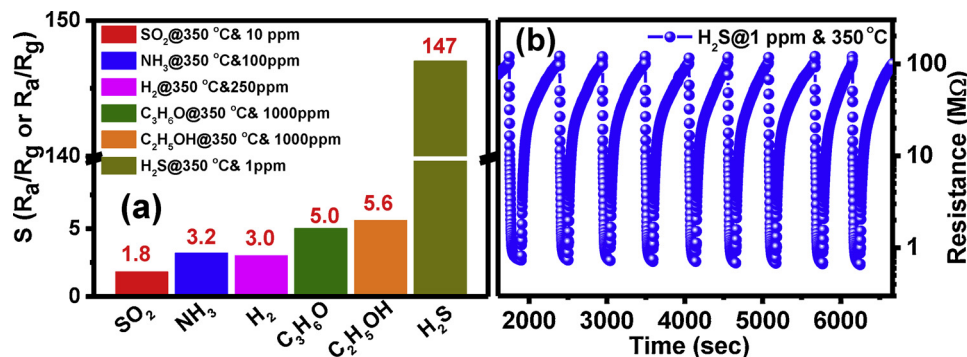


Fig. 10. Selectivity to various gases at 350 °C (a) and stability at 1 ppm H₂S gas at 350 °C (b) of the sensors based on the 1 wt.% RGO-loaded ZnFe₂O₄ NFs calcined at 600 °C.

annealing temperature as stated in previous reports [25,27]. In addition, when the annealing temperature decreases, the weight loss of RGO also decreases (Figure S1c) and the rest of the RGO amount is enlarged. As a result, the response of the 1.0 wt% RGO-loaded ZFO NF sensor varies when the annealing temperature changes. The response and recovery times as functions of annealing temperatures are displayed in Fig. 8f. The response time remains almost unchanged when the annealing temperatures change. In contrast, the recovery time fluctuates with increased annealing temperatures from 400 to 700 °C because of the effects of nanograin size and RGO weight loss. Nanograins grow with increased annealing temperature (Fig. 2), leading to smaller grain boundaries. As a result, the recovery time decreases because the gas diffusion along grain boundaries becomes faster. Furthermore, the recovery time depends on the RGO content, which is changed by annealing temperature as discussed above. Therefore, at low annealing temperature of 400 °C, the weight loss of RGO is relatively small; RGO forms an individual conducting channel, leading to decreased recovery time. However, the recovery time sharply increases because of the grain growth, resulting in increased overall recovery time. The recovery time quickens with the increased annealing temperature of 500 °C because of major effects of grain growth; concurrently, the recovery time lengthens with further increased annealing temperature to 600 °C due to strong effects of greater RGO weight loss. With the high annealing temperature of 700 °C, the recovery time dramatically decreases due to strong grain growth and a decline in the number of absorbed H₂S gas because of the larger weight loss of RGO. The effects of nanograin size and RGO weight loss also explain the change in the sensor resistance as functions of annealing temperatures from 400 to 700 °C (Fig. 8g). The sensor resistance at 350 °C in air reaches a maximum at 600 °C. At the low annealing temperature of 400 °C, RGO weight loss is small, which leads to the formation of an individual conducting path of RGO nanosheets and thus decreases the sensor resistance. Meanwhile, at the high annealing temperature of 700 °C, the sensor resistance decreases because of increased electron mobility by grain growth.

The comparison of the effects of annealing temperatures on the response of the pure ZFO and 1.0 wt% RGO-loaded ZFO NF sensor is exhibited in Fig. 9a–b. The magnitude of the effects on the response of the RGO-loaded sensor significantly decreases with increased annealing temperatures from 400 to 700 °C due to increased weight loss of RGO. It is the same as the effects of annealing temperatures on the detection limit of the sensors based on pure ZFO NFs and 1.0 wt% RGO-loaded ZFO NFs (Fig. 9c). The detection limit (*DL*) is the lowest concentration of gas that can be distinguished by the sensor [28,49]. The *DL* is calculated as $DL = 3(rms_{noise}/slope)$ [49], where *rms_{noise}* is the root-mean-square deviation and *slope* is the slope value of the linear fit of the gas response versus gas concentration. The *rms_{noise}* can be calculated by 10 experimental data points at the baseline of the transient response for fifth polynomial curve-fitting. The results of *DL* calculations are shown in Figure S3 and Table S1 (Supporting Information). RGO decrease the *DL* of RGO-loaded sensors when compared to that of pure ZFO sensor, but the level of the effects on the *DL* of RGO-loaded sensors significantly decreases with increased annealing temperatures.

The effects of annealing temperatures on the response and recovery times of the sensors based on pure ZFO NFs and 1.0 wt% RGO-loaded ZFO NFs are quite different due to the change in RGO weight loss with various annealing temperatures (Fig. 9d). In general, the response and recovery time of the former are longer than those of the latter because of the larger electron mobility in RGO-loaded sensors.

The selectivity, stability and the effects of ambient relative humidity are important issues for practical applications. The selectivity of the 1.0 wt% RGO-loaded ZFO NF sensor calcined at 600 °C was investigated by testing a wide range of interference gases. The gas responses to 10 ppm SO₂, 100 ppm NH₃, 250 ppm H₂, 1000 ppm acetone and 1000 ppm ethanol gas were calculated from the transient response (see Supporting Information, Figure S4) as displayed in Fig. 9a. It is obvious that the sensors exhibit the highest response to H₂S gas, much higher

than their responses to the interfering gases despite the fact that the concentrations of the interfering gases are a thousand times higher than that of H₂S gas. This result reveals that the RGO-loaded ZFO NF sensor has good selectivity to H₂S gas. The results are quite similar to some previous reports [3,4,24]. The short-term stability of the sensor was also tested with nine cycles to 1 ppm H₂S at 350 °C and the result is shown in Fig. 10b. The sensor can maintain its initial response amplitude with nine continuous response/recovery cycles. The result indicates that the sensor has good reproducibility and short-term stability. Additionally, the effects of ambient relative humidity (RH) on the response of the sensor based on 1.0 wt% RGO-loaded ZFO NF calcined at 600 °C to 1 ppm H₂S gas at the working temperature of 350 °C were also investigated (Figure S5 in Supporting Information). RH does not have any impact on gas response at low relative humidity between 40 and 70%. However, the response strongly goes down from 144 to 100 when RH is increased from 70% to 99%, which can be explained by the occupation of chemisorbed and physisorbed water on the active sites of the NFs [18].

4. Conclusions

The sensors based on RGO-loaded ZFO NFs have been successfully synthesized by electrospinning and then calcined at different annealing temperatures. The NFs have diameters of 50 – 100 nm and consist of many nanograins. The gas sensing results show that the 1.0 wt% RGO-loaded ZFO NF sensor calcined at 600 °C has the best response to H₂S gas at selected gas concentration and working temperature ranges. The sensor responses reach 147 and 4.6 to 1 and 0.1 ppm H₂S gas, respectively, at the working temperature of 350 °C, which are higher than those of the pure ZFO sensor in the same conditions. The enhanced sensor responses are obtained because of the heterojunction between RGO and ZFO and the fact that the NFs comprise many nanograins resulting in a multi-porous structure and the formation of potential barriers at grain boundaries.

Acknowledgements

This work was supported by the Vietnam National Foundation for Science and Technology Development (NAFOSTED) under grant number 103.02-2017.25. Inkyu Park was also acknowledged for the supports from Multi-Ministry Collaborative R&D Program (Development of Techniques for Identification and Analysis of Gas Molecules to Protect Against Toxic Substances) through the National Research Foundation of Korea (NRF) funded by KNPA, MSIT, MOTIE, ME, NFA (NRF-2017M3D9A1073858).

Appendix A. Supplementary data

Supplementary material related to this article can be found, in the online version, at doi:<https://doi.org/10.1016/j.snb.2018.11.157>.

References

- [1] M.M. Rahman, S.B. Khan, M. Faisal, A.M. Asiri, K.A. Alamry, Highly sensitive formaldehyde chemical sensor based on hydrothermally prepared spinel ZnFe₂O₄ nanorods, *Sens. Actuators B Chem.* 171 (172) (2012) 932–937, <https://doi.org/10.1016/j.snb.2012.06.006>.
- [2] R.C.V. Gopal, S.V. Manorama, V.J. Rao, C.V.G. Reddy, Preparation and characterization of ferrites as gas sensor materials, *J. Mater. Sci. Lett.* 9 (2000) 775–778, <https://doi.org/10.1023/A:1006716721984>.
- [3] G. Ximing, Y. Sun, C. Zhu, C. Li, Q. Ouyang, Y. Chen, Highly sensitive and selective H₂S sensor based on porous ZnFe₂O₄ nanosheets, *Sens. Actuators B Chem.* 193 (2014) 501–508, <https://doi.org/10.1016/j.snb.2013.11.072>.
- [4] J. Wu, D. Gao, T. Sun, J. Bi, Y. Zhao, Z. Ning, G. Fan, Z. Xie, Highly selective gas sensing properties of partially inverted spinel zinc ferrite towards H₂S, *Sens. Actuators B Chem.* 235 (2016) 258–262, <https://doi.org/10.1016/j.snb.2016.05.083>.
- [5] A. Sutka, K.A. Gross, Spinel ferrite oxide semiconductor gas sensors, *Sens. Actuators B Chem.* 222 (2016) 95–105, <https://doi.org/10.1016/j.snb.2015.08.027>.

- [6] A. Mirzaei, S.S. Kim, H.W. Kim, Resistance-based H₂S gas sensors using metal oxide nanostructures: a review of recent advances, *J. Hazard. Mater.* 357 (2018) 314–331, <https://doi.org/10.1016/j.jhazmat.2018.06.015>.
- [7] H.W. Kim, A. Mirzaei, S. Sub, H. Woo, Resistance-based H₂S gas sensors using metal oxide nanostructures: a review of recent advances, *J. Hazard. Mater.* 357 (2018) 314–331, <https://doi.org/10.1016/j.jhazmat.2018.06.015>.
- [8] Z. Guo, G. Chen, G. Zeng, C. Zhang, RSC Advances Metal oxides and metal salt nanostructures for hydrogen sulfide sensing: mechanism and sensing performance, *RSC Adv.* 5 (2015) 54793–54805, <https://doi.org/10.1039/C5RA10394K>.
- [9] S.K. Pandey, K.-H. Kim, K.-T. Tang, A review of sensor-based methods for monitoring hydrogen sulfide, *TrAC Trends Anal. Chem.* 32 (2012) 87–99, <https://doi.org/10.1016/j.trac.2011.08.008>.
- [10] E. Llobet, J. Brunet, A. Pauly, A. Ndiaye, C. Varenne, Nanomaterials for the selective detection of hydrogen sulfide in air, *Sensors* 17 (2017) 391, <https://doi.org/10.3390/s17020391>.
- [11] J. Shi, Z. Cheng, L. Gao, Y. Zhang, J. Xu, H. Zhao, Facile synthesis of reduced graphene oxide/hexagonal WO₃ nanosheets composites with enhanced H₂S sensing properties, *Sens. Actuators B Chem.* 230 (2016) 736–745, <https://doi.org/10.1016/j.snb.2016.02.134>.
- [12] S. Bai, C. Chen, R. Luo, A. Chen, D. Li, Synthesis of MoO₃/reduced graphene oxide hybrids and mechanism of enhancing H₂S sensing performances, *Sens. Actuators B Chem.* 216 (2015) 113–120, <https://doi.org/10.1016/j.snb.2015.04.036>.
- [13] S.-J. Choi, B.-H. Jang, S.-J. Lee, B.K. Min, A. Rothschild, I.-D. Kim, Selective detection of acetone and hydrogen sulfide for the diagnosis of diabetes and halitosis using SnO₂ nanofibers functionalized with reduced graphene oxide nanosheets, *ACS Appl. Mater. Interfaces* 6 (2014) 2588–2597, <https://doi.org/10.1021/am405088q>.
- [14] Z. Jiang, J. Li, H. Aslan, Q. Li, Y. Li, M. Chen, Y. Huang, J.P. Fröning, M. Otyepka, R. Zboril, F. Besenbacher, M. Dong, A high efficiency H₂S gas sensor material: paper like Fe₂O₃/graphene nanosheets and structural alignment dependency of device efficiency, *J. Mater. Chem. A Mater. Energy Sustain.* 2 (2014) 6714, <https://doi.org/10.1039/c3ta15180h>.
- [15] H. Qiao, Z. Xia, Y. Fei, L. Cai, R. Cui, Y. Cai, Q. Wei, Q. Yao, Electrospinning combined with hydrothermal synthesis and lithium storage properties of ZnFe₂O₄-graphene composite nanofibers, *Ceram. Int.* 43 (2017) 2136–2142, <https://doi.org/10.1016/j.ceramint.2016.10.194>.
- [16] R. Ramaseshan, S. Sundarajan, R. Jose, S. Ramakrishna, Nanostructured ceramics by electrospinning, *J. Appl. Phys.* 102 (2007), <https://doi.org/10.1063/1.2815499>.
- [17] T. Hu, X. Chu, F. Gao, Y. Dong, W. Sun, L. Bai, Trimethylamine sensing properties of graphene quantum Dots/α-Fe₂O₃ composites, *J. Solid State Chem.* 237 (2016) 284–291, <https://doi.org/10.1016/j.jssc.2016.02.037>.
- [18] L. Guo, X. Kou, M. Ding, C. Wang, Al. Dong, H. Zhang, C. Feng, Y. Sun, Y. Gao, P. Sun, G. Lu, Reduced graphene oxide/α-Fe₂O₃ composite nanofibers for application in gas sensors, *Sens. Actuators B Chem.* 244 (2017) 233–242, <https://doi.org/10.1016/j.snb.2016.12.137>.
- [19] J.H. Lee, A. Katoch, S.W. Choi, J.H. Kim, H.W. Kim, S.S. Kim, Extraordinary improvement of gas-sensing performances in SnO₂ nanofibers due to creation of local p-n heterojunctions by loading reduced graphene oxide nanosheets, *ACS Appl. Mater. Interfaces* 7 (2015) 3101–3109, <https://doi.org/10.1021/am5071656>.
- [20] Z.U. Abideen, J.Y. Park, H.W. Kim, S.S. Kim, Graphene-loaded tin oxide nanofibers: optimization and sensing performance, *Nanotechnology* 28 (2017), <https://doi.org/10.1088/1361-6528/28/3/035501>.
- [21] Q. Feng, X. Li, J. Wang, A.M. Gaskov, Reduced graphene oxide (rGO) encapsulated Co₂O₄ composite nanofibers for highly selective ammonia sensors, *Sens. Actuators B Chem.* 222 (2016) 864–870, <https://doi.org/10.1016/j.snb.2015.09.021>.
- [22] Z.U. Abideen, A. Katoch, J.H. Kim, Y.J. Kwon, H.W. Kim, S.S. Kim, Excellent gas detection of ZnO nanofibers by loading with reduced graphene oxide nanosheets, *Sens. Actuators B Chem.* 221 (2015) 1499–1507, <https://doi.org/10.1016/j.snb.2015.07.120>.
- [23] Z.U. Abideen, H.W. Kim, S.S. Kim, An ultra-sensitive hydrogen gas sensor using reduced graphene oxide-loaded ZnO nanofibers, *Chem. Commun. (Camb.)* 51 (2015) 15418–15421, <https://doi.org/10.1039/C5CC05370F>.
- [24] F. Liu, X. Chu, Y. Dong, W. Zhang, W. Sun, L. Shen, Acetone gas sensors based on graphene-ZnFe₂O₄ composite prepared by solvothermal method, *Sens. Actuators B Chem.* 188 (2013) 469–474, <https://doi.org/10.1016/j.snb.2013.06.065>.
- [25] A. Katoch, G.J. Sun, S.W. Choi, J.H. Byun, S.S. Kim, Competitive influence of grain size and crystallinity on gas sensing performances of ZnO nanofibers, *Sens. Actuators B Chem.* 185 (2013) 411–416, <https://doi.org/10.1016/j.snb.2013.05.030>.
- [26] J.Y. Park, K. Asokan, S.W. Choi, S.S. Kim, Growth kinetics of nanograins in SnO₂ fibers and size dependent sensing properties, *Sens. Actuators B Chem.* 152 (2011) 254–260, <https://doi.org/10.1016/j.snb.2010.12.017>.
- [27] S.W. Choi, J.Y. Park, S.S. Kim, Growth behavior and sensing properties of nanograins in CuO nanofibers, *Chem. Eng. J.* 172 (2011) 550–556, <https://doi.org/10.1016/j.cej.2011.05.100>.
- [28] K. Anand, O. Singh, M.P. Singh, J. Kaur, R.C. Singh, Hydrogen sensor based on graphene/ZnO nanocomposite, *Sens. Actuators B Chem.* 195 (2014) 409–415, <https://doi.org/10.1016/j.snb.2014.01.029>.
- [29] Y. Xiao, Q. Yang, Z. Wang, R. Zhang, Y. Gao, P. Sun, Y. Sun, G. Lu, Improvement of NO₂ gas sensing performance based on discoid tin oxide modified by reduced graphene oxide, *Sens. Actuators B Chem.* 227 (2016) 419–426, <https://doi.org/10.1016/j.snb.2015.11.051>.
- [30] L. Tang, Y. Wang, Y. Li, H. Feng, J. Lu, J. Li, Preparation, structure, and electrochemical properties of reduced graphene sheet films, *Adv. Funct. Mater.* 19 (2009) 2782–2789, <https://doi.org/10.1002/adfm.200900377>.
- [31] Z. Fan, K. Wang, T. Wei, J. Yan, L. Song, B. Shao, An environmentally friendly and efficient route for the reduction of graphene oxide by aluminum powder, *Carbon* 48 (2010) 1686–1689, <https://doi.org/10.1016/j.carbon.2009.12.063>.
- [32] J. Zhang, H. Yang, G. Shen, P. Cheng, J. Zhang, S. Guo, Reduction of graphene oxide via L-ascorbic acid, *Chem. Commun. (Camb.)* 46 (2010) 1112–1114, <https://doi.org/10.1039/b917705a>.
- [33] H. Zhang, L. Yu, Q. Li, Y. Du, S. Ruan, Reduced graphene oxide/α-Fe₂O₃ hybrid nanocomposites for room temperature NO₂ sensing, *Sens. Actuators B Chem.* 241 (2017) 109–115, <https://doi.org/10.1016/j.snb.2016.10.059>.
- [34] S. Stankovich, D.A. Dikin, R.D. Piner, K.A. Kohlhaas, A. Kleinhammes, Y. Jia, Y. Wu, S.T. Nguyen, R.S. Ruoff, Synthesis of graphene-based nanosheets via chemical reduction of exfoliated graphite oxide, *Carbon* 45 (2007) 1558–1565, <https://doi.org/10.1016/j.carbon.2007.02.034>.
- [35] Z. Bo, X. Shuai, S. Mao, H. Yang, J. Qian, J. Chen, J. Yan, K. Cen, Green preparation of reduced graphene oxide for sensing and energy storage applications, *Sci. Rep.* 4 (2014) 4684, <https://doi.org/10.1038/srep04684>.
- [36] P. Cui, J. Lee, E. Hwang, H. Lee, One-pot reduction of graphene oxide at subzero temperatures, *Chem. Commun. (Camb.)* 47 (2011) 12370, <https://doi.org/10.1039/c1cc15569e>.
- [37] Y. Zhou, Q. Bao, L.A.L. Tang, Y. Zhong, K.P. Loh, Hydrothermal dehydration for the “green” reduction of exfoliated graphene oxide to graphene and demonstration of tunable optical limiting properties, *Chem. Mater.* 21 (2009) 2950–2956, <https://doi.org/10.1021/cm9006603>.
- [38] M. Iliut, C. Leordean, V. Canpean, C.-M. Teodorescu, S. Astilean, A new green, ascorbic acid-assisted method for versatile synthesis of Au-graphene hybrids as efficient surface-enhanced Raman scattering platforms, *J. Mater. Chem. C Mater. Opt. Electron. Devices* 1 (2013) 4094–4104, <https://doi.org/10.1039/C3TC30177J>.
- [39] A.C. Ferrari, J. Robertson, Interpretation of Raman spectra of disordered and amorphous carbon, *Phys. Rev. B* 61 (2000) 14095–14107, <https://doi.org/10.1103/PhysRevB.61.14095>.
- [40] M. Fu, Q. Jiao, Y. Zhao, In situ fabrication and characterization of cobalt ferrite nanorods/graphene composites, *Mater. Charact.* 86 (2013) 303–315, <https://doi.org/10.1016/j.matchar.2013.10.019>.
- [41] K. Satheesh, R. Jayavel, Synthesis and electrochemical properties of reduced graphene oxide via chemical reduction using thiourea as a reducing agent, *Mater. Lett.* 113 (2013) 5–8, <https://doi.org/10.1016/j.matlet.2013.09.044>.
- [42] M. Zong, Y. Huang, H. Wu, Y. Zhao, Q. Wang, X. Sun, One-pot hydrothermal synthesis of RGO/CoFe₂O₄ composite and its excellent microwave absorption properties, *Mater. Lett.* 114 (2014) 52–55, <https://doi.org/10.1016/j.matlet.2013.09.113>.
- [43] H. Zhang, A. Xie, C. Wang, H. Wang, Y. Shen, X. Tian, Novel rGO/α-Fe₂O₃ composite hydrogel: synthesis, characterization and high performance of electromagnetic wave absorption, *J. Mater. Chem. A Mater. Energy Sustain.* 1 (2013) 8547, <https://doi.org/10.1039/c3ta11278k>.
- [44] J. Wu, D. Gao, T. Sun, J. Bi, Y. Zhao, Z. Ning, G. Fan, Z. Xie, Highly selective gas sensing properties of partially inverted spinel zinc ferrite towards H₂S, *Sens. Actuators B Chem.* 235 (2016) 258–262, <https://doi.org/10.1016/j.snb.2016.05.083>.
- [45] R.J. Zou, G.J. He, K.B. Xu, Q. Liu, Z.Y. Zhang, J.Q. Hu, ZnO nanorods on reduced graphene sheets with excellent field emission, gas sensor and photocatalytic properties, *J. Mater. Chem. A Mater. Energy Sustain.* 1 (2013) 8445–8452, <https://doi.org/10.1039/c3ta11490b>.
- [46] S. Singkammo, A. Wisitsoraat, C. Sriprachubwong, A. Tuantranont, S. Phanichphant, C. Liewhiran, Electrolytically exfoliated graphene-loaded flame-made Ni-doped SnO₂ composite film for acetone sensing, *ACS Appl. Mater. Interfaces* 7 (2015) 3077–3092, <https://doi.org/10.1021/acsami.5b00161>.
- [47] B. Zhang, J. Liu, X. Cui, Y. Wang, Y. Gao, P. Sun, F. Liu, K. Shimano, N. Yamazoe, G. Lu, Enhanced gas sensing properties to acetone vapor achieved by α-Fe₂O₃ particles ameliorated with reduced graphene oxide sheets, *Sens. Actuators B Chem.* 241 (2017) 904–914, <https://doi.org/10.1016/j.snb.2016.11.023>.
- [48] N. Van Hoang, C. Manh, N. Duc, N. Van Duy, Facile on-chip electrospinning of ZnFe₂O₄ nanofiber sensors with excellent sensing performance to H₂S down ppb level, *J. Hazard. Mater.* 360 (2018) 6–16, <https://doi.org/10.1016/j.jhazmat.2018.07.084>.
- [49] L.A. Currie, Nomenclature in evaluation of analytical methods including detection and quantification capabilities (IUPAC Recommendations 1995), *Anal. Chim. Acta* 391 (1999) 105–126.